

Detecting Overfitting via Adversarial Examples

Roman Werpachowski, András György*, Csaba Szepesvári†
DeepMind
London, UK
{romanw, agyorgy, szepi}@google.com

March 3, 2022

Abstract

The repeated reuse of test sets in popular benchmark problems raises doubts about the credibility of reported test error rates. Verifying whether a learned model is overfitted to a test set is challenging as independent test sets drawn from the same data distribution are usually unavailable, while other test sets may introduce a distribution shift. We propose a new hypothesis test that uses only the original test data to detect overfitting. It utilizes a new unbiased error estimate that is based on adversarial examples generated from the test data and importance weighting. Overfitting is detected if this error estimate is sufficiently different from the original test error rate. The power of the method is illustrated using Monte Carlo simulations on a synthetic problem. We develop a specialized variant of our dependence detector for multiclass image classification, and apply it to testing overfitting of recent models to two popular real-world image classification benchmarks. In the case of ImageNet, our method was not able to detect overfitting to the test set for a state-of-the-art classifier, while on CIFAR-10 we found strong evidence of overfitting for the two recent model architectures we considered, and weak evidence of overfitting on the level of individual training runs.

1 Introduction

Deep neural networks achieve impressive performance on many important machine learning benchmarks, such as image classification (Krizhevsky, 2009; Krizhevsky et al., 2012; Szegedy et al., 2015; Simonyan and Zisserman, 2015; He et al., 2016), automated translation (Bahdanau et al., 2014; Wu et al., 2016) or speech recognition (Deng et al., 2013; Graves et al., 2013). However, the benchmark datasets are used a multitude of times by researchers worldwide. Since state-of-the-art methods are selected and published based on their performance on the corresponding test set, it is typical to see results that continuously improve over time; see, e.g., the discussion of Recht et al. (2018) and Figure 1 for the performance improvement of classifiers published for the popular CIFAR-10 image classification benchmark (Krizhevsky, 2009). This process may naturally lead to models overfitted to the test set, rendering test error rate (the average error measured on the test set) an unreliable indicator of the actual performance.

Detecting whether the model is overfitted to the test set is challenging, because independent test sets drawn from the same data distribution are generally not available, while alternative test sets often introduce a distribution shift.¹ The shift may happen even if the new test set is collected very carefully. For example, the recent CIFAR-10.1 dataset was collected by diligently following the original data curation procedure of CIFAR-10, and yet the data distribution underlying CIFAR-10.1 appears to be different from that of the test set of CIFAR-10 (for details, see Recht et al., 2018).

*A. György is also with Imperial College London, London, UK.

†Cs. Szepesvári is also with the University of Alberta, Edmonton, AB, Canada.

¹Throughout the paper we work with the standard statistical learning theory framework which assumes that data, both training and test, is sampled independently from a fixed underlying data distribution.

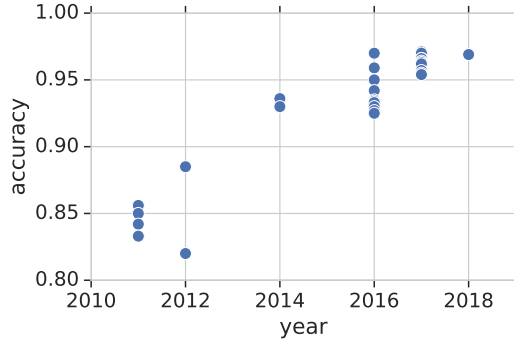


Figure 1: Accuracy of CIFAR-10 image classification models on CIFAR-10 test set, by year of publication (the data is taken from Recht et al., 2018).

To estimate the performance of a model on unseen data, one may use generalization bounds to get upper bounds on the expected error rate. The generalization bounds are also applicable when the model and the data are dependent (e.g., for error estimates based on the training data or the reused test data), but they usually lead to loose error bounds. Similarly, constructing confidence intervals around the training and test error rates from generalization bounds and rejecting independence of the test set if they do not overlap does not work in practice for the same reason. On the other hand, if the test data and the model are independent, much tighter bounds are available; hence, dependence testing can be applied to validate the resulting bounds. Recently, several methods that allow the reuse of the test set while keeping the validity of test error rates have been proposed (Dwork et al., 2015). However, these are *intrusive*: they require the user to follow a strict protocol of interacting with the test set and are thus not applicable in the more common situation when enforcing such a protocol is impossible.

In this paper we take a new approach to the challenge of detecting overfitting of a model to the test set. Our method is non-intrusive and uses only the original test data. The core novel idea is to harness the power of adversarial examples (Goodfellow et al., 2014) for our purposes. These are data points² which are not sampled from the data distribution, but instead are cleverly crafted based on existing data points so that the model errs on them. Several authors showed that the best models learned for the above-mentioned benchmark problems are highly sensitive to adversarial attacks (Goodfellow et al., 2014; Papernot et al., 2016; Uesato et al., 2018; Carlini and Wagner, 2017a;b; Papernot et al., 2017). For instance, one can often create adversarial versions of images properly classified by a state-of-the-art model that the model will make a mistake on. Often, the adversarial versions are (almost) indistinguishable from the original for a human observer, see for example Figure 2, where the adversarial image is obtained from the original one by a carefully selected translation.

Most of the work on adversarial examples either concentrates on finding perturbation methods to create adversarial points that can fool classifiers (i.e., finding successful attack methods) or tries to train models that simultaneously have small test error rate and small error on adversarial modifications of the test set (which we will refer to as the adversarial error rate) (Gu and Rigazio, 2014; Cisse et al., 2017; Liao et al., 2017; Kolter and Wong, 2017; Madry et al., 2017; Kurakin and Goodfellow, 2017; Tramèr et al., 2018). In this paper we are not directly interested in these issues, and use adversarial examples to create a new error estimator that is less sensitive to overfitting to the data. The estimator uses adversarial examples together with importance weighting to take into account the change in the data distribution (covariate shift) due to the adversarial transformation. The obtained estimator, which we call the *adversarial (error) estimator*,³ is unbiased and has a smaller variance than the standard test error rate if the test set and the model are independent.

²Throughout the paper, we use the words “example” and “point” interchangeably.

³Note that the adversarial error estimator’s goal is to estimate the error rate, not the adversarial error rate.



scale, weighing machine



toaster

Figure 2: Adversarial example for the ImageNet dataset generated by a $(5, -5)$ translation: the original example (left) is correctly classified as “scale, weighing machine,” the adversarially generated example (right) is classified as “toaster,” while the image class is the same for any human observer.

More importantly, since it is based on adversarially generated data points, the adversarial estimator is expected to differ significantly from the test error rate if the model is overfitted to the test set, providing a way to detect test set overfitting. Thus, the test error rate and the adversarial error estimate (calculated based on the same test set) must be close if the test set and the model are independent, and are expected to be different in the opposite case. In particular, if the gap between the two error estimates is large, the independence hypothesis (i.e., that the model and the test set are independent) is dubious and will be rejected. Combining results from multiple training runs, we develop another method to test overfitting of a model architecture.⁴ The most challenging aspect of our method is to construct adversarial perturbations for which we can calculate importance weights, while keeping enough degrees of freedom in the way the adversarial perturbations are generated to maximize power, the ability of the test to detect dependence when it is present.

We apply our independence tests to state-of-the-art classification methods for two popular image classification benchmarks, ImageNet (Deng et al., 2009) and CIFAR-10 (Krizhevsky, 2009). Considering VGG-like image-classification models (Simonyan and Zisserman, 2015; Rosca et al., 2017), we found that the independence hypothesis cannot be rejected for ImageNet at almost any confidence level, which is a strong evidence that the VGG-like model is not overfitted to the test set (as a control experiment, we verify that the independence of the trained classifier and the training set is rejected with high confidence). For CIFAR-10, our individual test rejects the independence of a trained model and the test set at a confidence level of about 40%.⁵ While this result is inconclusive, the independence of the CIFAR-10 test set and the *model architecture* can be rejected at a convincing confidence level of 97%. Similar results are obtained for the Wide Residual Network (WideResnet) architecture of Zagoruyko and Komodakis (2016). In conclusion, our method provides strong evidence for overfitting of the tested architectures to the test set, but the effect is much harder to detect for an individual training run, most likely due to the stochastic nature of the training process. As a sanity check, our individual independence test verifies (i.e., does not reject) the independence of the individual VGG models and the truly independent CIFAR-10.1 test set (on average, the independence can be rejected at a negligible confidence level of about 7%, while for about 80% of the individual models, independence cannot be rejected at any confidence level), while the independence of the model architecture can only be rejected at a confidence level of about 30%. Unfortunately, these latter results are less meaningful in the sense that similar confidence levels can be obtained if the test is applied to randomly selected subsets of the CIFAR-10 test set with the same size (2000 images) .

⁴Note that by model architecture we mean not just the layout of the architecture, e.g., that of a neural network, but also the corresponding training procedure and its (hyper-)parameters, except for the random seed.

⁵To be precise, we consider a rescaled version of the CIFAR-10 dataset; see Section 5.3 for details.

The rest of the paper is organized as follows: In Section 2, we introduce a formal model for error estimation using adversarial examples, including the definition of adversarial example generators. The new overfitting-detection tests are derived in Section 3. To gain better understanding of their behavior, the tests are first analyzed on a synthetic example using Monte Carlo simulation in Section 4, while their application to image-classification benchmarks is presented in Section 5. Finally, conclusions are drawn and further research questions are discussed in Section 6.

2 Adversarial Risk Estimation

We consider a classification problem with deterministic (noise-free) labels, which is a reasonable assumption for many practical problems, such as image recognition (we leave the extension of our method to noisy labels for future work). In particular, let \mathcal{X} denote the input space and $\mathcal{Y} = \{0, \dots, K - 1\}$ the set of labels. For simplicity, we assume that $\mathcal{X} \subset \mathbb{R}^D$. Data is sampled from the distribution \mathcal{P} over \mathcal{X} ,⁶ and the class label is determined by a function $f^* : \mathcal{X} \rightarrow \mathcal{Y}$, which we refer to as the *ground truth*. We denote a random vector drawn from \mathcal{P} by X , and its corresponding class label by $Y = f^*(X)$. We consider deterministic classifiers of the form $f : \mathcal{X} \rightarrow \mathcal{Y}$, which assign a deterministic label $f(X)$ to every value of X . The performance is measured by the zero-one loss, that is, the loss of f classifying $x \in \mathcal{X}$ is $L(f, x) = \mathbb{I}(f(x) \neq f^*(x))$,⁷ and the *expected error* (also known as the *risk* or *expected risk* in the learning theory literature) of the classifier f is defined as

$$R(f) = \mathbb{P}(f(X) \neq Y) = \mathbb{E}[\mathbb{I}(f(X) \neq Y)] = \mathbb{E}[L(f, X)] = \int_{\mathcal{X}} L(f, x) d\mathcal{P}(x) .$$

Consider a test dataset $S = \{(X_1, Y_1), \dots, (X_m, Y_m)\}$ where the X_i are drawn from \mathcal{P} independently of each other and $Y_i = f^*(X_i)$.⁸ In the learning setting, the classifier f usually also depends on some randomly drawn training data and, as such, is random itself. If f is independent from S , then $L(f, X_1), \dots, L(f, X_m)$ are independent and identically distributed, and thus the empirical error rate

$$\hat{R}_S(f) = \frac{1}{m} \sum_{i=1}^m L(f, X_i) = \frac{1}{m} \sum_{i=1}^m \mathbb{I}(f(X_i) \neq Y_i) \quad (1)$$

is an unbiased estimate of $R(f)$ for all f , that is, $R(f) = \mathbb{E}[\hat{R}_S(f)|f]$. If f and S are not independent, the performance guarantees on the empirical estimates available in the independent case are significantly weakened because $L(f, X_1), \dots, L(f, X_m)$ may no longer be independent. For example, in case of overfitting to S , the empirical error rate is likely to be much smaller than the expected error. To detect the lack of independence and the potential bias of the empirical error rate, we construct alternate error (risk) estimators with their corresponding confidence intervals that are valid under the independence assumption. If the confidence intervals do not overlap sufficiently, we can reject the hypothesis that the sample S and the classifier f are independent.

As the first estimate, we use the test error rate $\hat{R}_S(f)$. To produce the other estimate, we use the well-known *importance sampling* or *change of measure* idea (Kahn and Harris, 1951): instead of sampling from the distribution \mathcal{P} , we sample from another distribution \mathcal{P}' and correct the estimate by appropriate reweighting. Assuming \mathcal{P} is absolutely continuous with respect to \mathcal{P}' on the set $E = \{x \in \mathcal{X} : L(f, x) \neq 0\}$,

$$R(f) = \int_{\mathcal{X}} L(f, x) d\mathcal{P}(x) = \int_E L(f, x) h(x) d\mathcal{P}'(x) , \quad (2)$$

⁶Throughout the paper we assume that the standard measurability assumptions are satisfied.

⁷For a Boolean-valued expression B , $\mathbb{I}(B)$ denotes its indicator function, that is, $\mathbb{I}(B) = 1$ if B is true and $\mathbb{I}(B) = 0$ otherwise.

⁸Here, following the rest of the machine learning literature, we abuse notation. Technically, the sample should be seen as a sequence (not a set) drawn from the m -fold product of \mathcal{P} with itself, $(\mathcal{P})^{\otimes m}$.

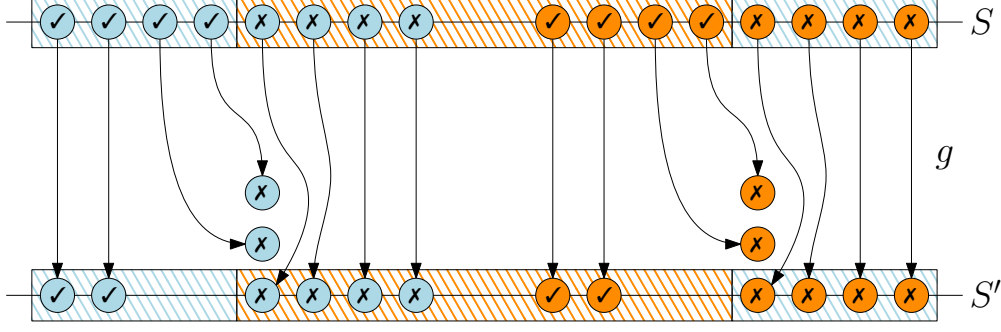


Figure 3: Generating adversarial examples. The top row depicts the original dataset S , with blue (B) and orange (O) points representing the two classes. The classifier’s prediction is represented by the striped areas: the four points on both sides are classified as B, while the middle points are classified as O (checkmarks and crosses denote if a point is correctly or incorrectly classified). The arrows show the adversarial transformations via the AEG g , resulting in the new dataset S' : Misclassified points are unchanged, while some correctly classified points are moved, but their original class label is unchanged. If the data is uniformly distributed over the original points, the transformation is density preserving, but not measure preserving: after the transformation the two rightmost correctly classified points in each class have probability 0, while the leftmost misclassified point in each class has probability $3/16$; hence, the Radon-Nikodym derivative for the latter points is $1/3$.

where $h = d\mathcal{P}/d\mathcal{P}'$ is the density (formally: Radon-Nikodym derivative) of \mathcal{P} with respect to \mathcal{P}' on E (h can be defined to have arbitrary finite values on $\mathcal{X} \setminus E$). It is well known that the variance of the estimator

$$\hat{R}'_{S'}(f) = \frac{1}{m} \sum_{i=1}^m L(f, X'_i) h(X'_i) = \frac{1}{m} \sum_{i=1}^m \mathbb{I}(f(X'_i) \neq Y'_i) h(X'_i) \quad (3)$$

obtained from a sample $S' = \{(X'_1, Y'_1), \dots, (X'_m, Y'_m)\}$ drawn independently from \mathcal{P}' is minimized if \mathcal{P}' is the so-called zero-variance importance sampling distribution defined by $d\mathcal{P}'(x) = (L(f, x)/R(f)) d\mathcal{P}(x)$ (see, e.g., Section 4.2 of Bucklew, 2004). That is, \mathcal{P}' is concentrated on E and $h(x) = R(f)/L(f, x)$ for all $x \in E$. In particular, in binary classification, $h(x) = R(f)$ for all $x \in E$.

Clearly, the zero-variance importance sampling distribution, and hence the above estimation strategy, is impossible to use, because it depends on the knowledge of both E and $R(f)$, the latter of which we want to estimate. Nevertheless, it suggests that to minimize the variance of an estimator $\hat{R}'_{S'}(f)$, S' needs to concentrate on points where f makes mistakes. In the next subsection we use the notion of adversarial examples to generate such distributions.

2.1 Generating adversarial examples

In this section we introduce a formal framework for generating adversarial examples. Given a classification problem instance with data distribution \mathcal{P} and ground truth f^* , an *adversarial example generator* (AEG) g for a classifier f is a (measurable) mapping $g : \mathcal{X} \rightarrow \mathcal{X}$ such that

- (G1) g preserves the class labels of the samples, that is, $f^*(x) = f^*(g(x))$ for \mathcal{P} -almost all x ; and
- (G2) g does not change points that are incorrectly classified by f , that is, $g(x) = x$ if $f(x) \neq f^*(x)$ for \mathcal{P} -almost all x .

A simple example that illustrates AEGs is given in Figure 3, while another example is presented in Section 4. The justification of the definition of AEGs, in relation to the existing literature, is as follows: An adversarial example is usually generated by staying in a small vicinity of the input, i.e., by keeping $d(x, g(x))$ small for some $d : \mathcal{X} \times \mathcal{X} \rightarrow [0, \infty)$ distance(-like) function, such as $d(x, y) = \|\cdot\|$ where $\|\cdot\|$

is, e.g., the 2- or the max-norm. We view this as a practical way of ensuring condition (G1), the idea being that for all points in the support of \mathcal{P} , by moving the point by a small amount, say, $\varepsilon > 0$, the label associated with the point is not going to change. If the label did change, the adversarial example generators proposed in the literature would not make sense. Thus, we can view condition (G1) as a relaxation of the foundational (implicit) assumption made in the literature underlying adversarial example generators. When developing practical methods for image recognition in Section 5, we also return to this stronger assumption instead of condition (G1). Note that this implicit assumption implies that the ε -boundary $B_\varepsilon = \{x' : \exists x_+, x_- \text{ s.t. } d(x_+, x'), d(x_-, x') \leq \varepsilon \text{ and } f^*(x_+) = 1, f^*(x_-) = 0\}$ has zero \mathcal{P} -measure — a geometric margin assumption. If the set B_ε does not have a zero measure, the error metrics that use AEGs can be biased in proportion to $\mathcal{P}(B_\varepsilon)$. It follows that as long as the probability of seeing examples on the ε -boundary between the positive and negative examples is negligible compared to whatever error estimates the methods produce, the conclusions remain valid. (G2) formalizes the fact that there is no need to change samples which are already misclassified. Indeed, existing AEGs comply with this condition.

The performance of an AEG is usually measured by how successfully it generates examples that are misclassified, which can be captured by

$$p_g = \mathbb{P}(f(g(X)) \neq f^*(g(X)) | f(X) = f^*(X)).$$

Accordingly, we call a point $g(x)$ a *successful adversarial example* if x is correctly classified by f and $f(g(x)) \neq f(x)$ (i.e., $L(f, x) = 0$ and $L(f, g(x)) = 1$).

In the development of our AEGs for image recognition tasks, we will make use of another condition. For simplicity, we formulate this condition for distributions \mathcal{P} that have a density ρ with respect to the uniform measure on \mathcal{X} , which is assumed to exist (notable cases are when \mathcal{X} is finite, or $\mathcal{X} = [0, 1]^D$ or when $\mathcal{X} = \mathbb{R}^D$; in the latter two cases the uniform measure is the Lebesgue measure). The assumption states that the AEG needs to be *density-preserving* in the sense that

$$(G3) \quad \rho(x) = \rho(g(x)) \text{ for } \mathcal{P}\text{-almost all } x.$$

Note that a density-preserving map may not be measure-preserving (the latter means that for all measurable $A \subset \mathcal{X}$, $\mathcal{P}(A) = \mathcal{P}(g(A))$).

We expect (G3) to hold when g perturbs its input by a small amount and if ρ is sufficiently smooth. We believe that the assumption is reasonable for, e.g., image recognition problems (at least in its relaxed form) where we expect that very close images will have a similar likelihood as measured by ρ . An AEG employing image translations, which satisfies (G3), will be introduced in Section 5. Both (G1) and (G3) can be relaxed (to a soft margin condition or allowing a slight change in ρ , resp.) at the price of an extra error term in the analysis that follows.

For a fixed AEG $g : \mathcal{X} \rightarrow \mathcal{X}$, let \mathcal{P}_g denote the distribution of $g(X)$ where $X \sim \mathcal{P}$ (\mathcal{P}_g is known as the pushforward measure of \mathcal{P} under g). Further, let $h_g = \frac{d\mathcal{P}}{d\mathcal{P}_g}$ on $E = \{x : L(f, x) \neq 0\}$ and arbitrary otherwise. It is easy to see that h_g is well-defined (on E) and, in addition, $h_g \leq 1$: First note that

$$\mathcal{P}_g(A) = \mathbb{P}(g(X) \in A) \geq \mathbb{P}(g(X) \in A, X \in E) = \mathbb{P}(X \in A) = \mathcal{P}(A)$$

where the second to last equality holds because $g(X) = X$ for any $X \in E$ under condition (G2). Thus, $\mathcal{P}(A) \leq \mathcal{P}_g(A)$ for any measurable $A \subset E$, which implies that h_g is well-defined on E and $h_g(x) \leq 1$ for all $x \in E$.

One may think that (G3) implies that $h_g(x) = 1$ for all $x \in E$. However, this does not hold. For example, if \mathcal{P} is a uniform distribution, any $g : \mathcal{X} \rightarrow \text{supp } \mathcal{P}$ satisfies (G3), where $\text{supp } \mathcal{P} \subset \mathcal{X}$ denotes the support of the distribution \mathcal{P} . This is also illustrated in Figure 3.

2.2 Risk estimation via adversarial examples

Combining the ideas of this section so far, we now introduce unbiased risk estimates based on adversarial examples. Our goal is to estimate the error-rate of f through an adversarially generated sample

$S' = \{(X'_1, Y_1), \dots, (X'_m, Y_m)\}$ obtained through an AEG g , where $X'_i = g(X_i)$ with X_1, \dots, X_m drawn independently from \mathcal{P} and $Y_i = f^*(X_i)$. Since g satisfies (G1) by definition, the original example X_i and the corresponding adversarial example X'_i have the same label Y_i . Recalling that $h_g = d\mathcal{P}/d\mathcal{P}_g \leq 1$ on $E = \{x \in \mathcal{X} : L(f, x) = 1\}$, we immediately see that the importance weighted adversarial estimate

$$\widehat{R}_g(f) = \frac{1}{m} \sum_{i=1}^m \mathbb{I}(f(X'_i) \neq Y_i) h_g(X'_i) \quad (4)$$

obtained from (3) for the adversarial sample S' has smaller variance than that of the empirical average $\widehat{R}_S(f)$: both estimates are unbiased with expectation $\mathbb{E}[\widehat{R}_g(f)] = \mathbb{E}[\widehat{R}_S(f)] = R(f)$, and so

$$\begin{aligned} \mathbb{V}[\widehat{R}_g(f)] &= \frac{1}{m} (\mathbb{E}[L(f, g(X))^2 h_g(g(X))^2] - R(f)^2) \\ &\leq \frac{1}{m} (\mathbb{E}[L(f, g(X)) h_g(g(X))] - R^2(f)) = \frac{1}{m} (R(f) - R^2(f)) = \mathbb{V}[\widehat{R}_S(f)]. \end{aligned}$$

Intuitively, the more successful the AEG is (i.e., the more classification error it induces), the smaller the variance of the estimate $\widehat{R}_g(f)$ becomes. As the adversarial error probability $p_g = \mathbb{P}(f(g(X)) \neq f^*(g(X))) = \int_E (1/h_g) d\mathcal{P}$ becomes larger, h_g becomes smaller in general, so the inequality is likely to be strengthened.

3 Detecting overfitting

In this section we show how the risk estimates introduced in the previous section can be used to test the *independence hypothesis* that

(H) the sample S and the model f are independent.

If (H) holds, $\mathbb{E}[\widehat{R}_g(f)] = \mathbb{E}[\widehat{R}_S(f)] = R(f)$, and so the difference $T_{S,g}(f) = \widehat{R}_g(f) - \widehat{R}_S(f)$ is expected to be small. On the other hand, if f is overfitted to the dataset S (in which case $\widehat{R}_S(f) < R(f)$), we expect $\widehat{R}_S(f)$ and $\widehat{R}_g(f)$ to behave differently (the latter being less sensitive to overfitting) since (i) $\widehat{R}_g(f)$ depends also on examples previously unseen by the training procedure; (ii) the adversarial transformation g aims to increase the loss, countering the effect of overfitting; (iii) especially in high dimensional settings, in case of overfitting one may expect that there are misclassified points very close to the decision boundary of f which can be found by a carefully designed AEG. Therefore, intuitively, (H) can be rejected if $|T_{S,g}(f)|$ exceeds some appropriate threshold. The simplest way to determine the threshold is based on constructing confidence intervals for these estimator based on concentration inequalities, as discussed in Appendix A.

A smaller threshold for $|T_{S,g}(f)|$, and hence a more effective independence test, can be devised if instead of independently estimating the behavior of \widehat{R}_S and $\widehat{R}_g(f)$, one utilizes their apparent correlation. Indeed, $T_{S,g}(f)$ is the average of terms

$$\begin{aligned} T_{i,g}(f) &= L(f, g(X_i)) h_g(g(X_i)) - L(f, X_i) \\ &= (L(f, g(X_i)) h_g(g(X_i)) - R(f)) - (L(f, X_i) - R(f)), \end{aligned} \quad (5)$$

that is, $T_{S,g}(f) = (1/m) \sum_{i=1}^m T_{i,g}(f)$, and the two terms in $T_{i,g}(f)$ are typically highly correlated by the construction of g . Thus, we can apply the empirical Bernstein bound (Mnih et al., 2008) to the pairwise differences $T_{i,g}(f)$ to set a tighter threshold in the test: if the independence hypothesis (H) holds (i.e., S and f are independent), then for any $0 < \delta < 1$, with probability at least $1 - \delta$,

$$|T_{S,g}(f)| \leq B(m, \bar{\sigma}_T^2, \delta, U) \quad (6)$$

with

$$B(m, \sigma^2, \delta, U) = \sqrt{\frac{2\sigma^2 \ln(3/\delta)}{m}} + \frac{3U \ln(3/\delta)}{m}, \quad (7)$$

where $\bar{\sigma}_T^2 = (1/m) \sum_{i=1}^m (T_i(f) - T_{S,g}(f))^2$ is the empirical variance of the $T_{i,g}(f)$ terms, and U denotes the range of the $T_{i,g}(f)$ (that is, $T_{i,g}(f) \in [\alpha, \alpha + U]$ for some constant α), and we also used that the expectation of each $T_{i,g}(f)$, and hence that of $T_{S,g}(f)$, is zero. Since $h_g \leq 1$ if $L(f, x) = 1$ (as discussed in Section 2.2), it follows that $U \leq 2$, but further assumptions (such as g being density preserving) can result in tighter bounds.

This leads to our pairwise dependence detection method:

$$\text{if } |T_{S,g}(f)| > B(m, \bar{\sigma}_T^2, \delta, 2), \text{ reject (H) at a confidence level } 1 - \delta \text{ (p-value } \delta).$$

Note that in order for the test to work well, we not only need the test statistic $T_{S,g}(f)$ to have a small variance in case of independence (this could be achieved if g were the identity), but we also need the estimators $\hat{R}_S(f)$ and $\hat{R}_g(f)$ behave sufficiently differently if the independence assumption is violated. The latter behavior is encouraged by stronger AEGs, as we will show empirically in Section 5.2 (see Figure 8 in particular).

Note that in order for the test to work well, we not only need the test statistic $T_{S,g}(f)$ to have a small variance in case of independence (this could be achieved if g were the identity), but we also need the estimators $\hat{R}_S(f)$ and $\hat{R}_g(f)$ behave sufficiently differently if the independence assumption is violated. The latter behavior is encouraged by stronger AEGs, as we will show empirically in Section 5.2 (see Figure 8 in particular).

For a given statistic $(|T_{S,g}(f)|, \bar{\sigma}_T^2)$, the largest confidence level (smallest p -value) at which (H) can be rejected can be calculated by setting the value of the statistic $|T_{S,g}(f)| - B(m, \bar{\sigma}_T^2, \delta, 2)$ to zero and solving for δ . This leads to the following formula for the p -value (if the solution is larger than 1, which happens when the bound (6) is loose, δ is capped at 1):

$$\delta = \min \left\{ 1, 3e^{-\frac{m}{9U^2} \left(\bar{\sigma}_T^2 + 3U|T_{S,g}(f)| - \bar{\sigma}_T \sqrt{\bar{\sigma}_T^2 + 6U|T_{S,g}(f)|} \right)} \right\}. \quad (8)$$

The main challenge in applying the method in practice is to find suitable AEG functions g for which we can compute the density h_g .

3.1 Dependence detector for randomized training

The dependence between the model and the test set can arise from (i) selecting the “best” random seed in order to improve the test set performance and/or (ii) tweaking the model architecture (e.g., neural network structure) and hyperparameters (e.g., learning-rate schedule). If one has access to a single instance of a trained model, these two sources cannot be disentangled. However, if the model architecture and training procedure is fully specified and computational resources are adequate, it is possible to isolate (i) and (ii) by retraining the model multiple times and calculating the p -value for every training run separately. Assuming N models, let $f_j, j = 1, \dots, N$ denote the j -th trained model and p_j the p -value calculated using the pairwise independence test (6) (i.e., from Eq. 8). We can investigate the degree to which (i) occurs by comparing the p_j values with the corresponding test set error rates $R_S(f_j)$. To investigate whether (ii) occurs, we can average over the randomness of the training runs.

For every example $X_i \in S$, consider the average test statistic

$$\bar{T}_i = \frac{1}{N} \sum_{j=1}^N T_i(f_j) = \frac{1}{N} \sum_{j=1}^N (L(f_j, g_j(X_i)) h_{g_j}(g_j(X_i)) - L(f_j, X_i))$$

where $T_i(f_j)$ is the statistic (5) calculated for example X_i and model f_j with AEG g_j selected for model f_j (note that AEGs are model-dependent by construction). If, for each i and j , the random variables $T_i(f_j)$ are independent, then so are \bar{T}_i (for all i). Hence, we can apply the pairwise dependence detector (6) with \bar{T}_i instead of T_i , using the average $\bar{T}_S = (1/m) \sum_{i=1}^m \bar{T}_i$ with empirical variance $\bar{\sigma}_{T,N}^2 = (1/m) \sum_{i=1}^m (\bar{T}_i - \bar{T}_S)^2$, giving a single p -value p_N . If the training runs vary enough in their outcomes, different models f_j will err on different data points in X_j , leading to $\bar{\sigma}_{T,N}^2 < \bar{\sigma}_T^2$ and therefore strengthening the power of the

dependence detector (indeed, our experiments in Section 5.3 on a CIFAR-10 image classification model show this behavior). This observation can also be interpreted in the following way: randomizing the training seed weakens the overfitting of the model architecture by introducing an important parameter which is not controlled in the experiments. Averaging the outcomes of $N \gg 1$ training runs removes this source of randomness, strengthening the dependence detector. On the other hand, if the random seed is “optimized” in order to improve the test set performance, then the above procedure is obviously not able to detect that.

Note that we can calculate \bar{T}_i also for a sequence of subsets of models of (e.g., size $N/10$ each), obtain a sequence of corresponding p -values and study their distribution. By changing the averaged model set size from 1 (testing every model independently) to N we adjust the trade-off between more information about the p -value distribution and detection power. To avoid reusing the same training run multiple times, given NK training runs we will calculate K statistics over N training run each, obtaining K p -values.

For brevity, we call this overfitting detection method (or, correspondingly, this test of independence) an N -model detector (or an N -model independence test).

4 Synthetic experiments

In this section we present a simple synthetic classification problem to illustrate the power of the method of Section 3. The benefit of this example is that we are able to compute the density h_g in an analytic form (see Figure 4 for an illustration).

Let $\mathcal{X} = \mathbb{R}^{500}$ and consider an input distribution with a density ρ that is an equally weighted mixture of two 500-dimensional isotropic truncated Gaussian distributions $N_{\pm}^{\text{trunc}}(\mu_{\pm}, \sigma^2 I)$ with coordinate-wise standard deviation $\sigma = \sqrt{500}$ (I denotes the identity matrix of size 500×500), means $\mu_{\pm} = [\pm 1, 0, 0, \dots, 0]$ and densities ρ_{\pm} truncated in the first dimension such that $\rho_+(x) = 0$ if $x_1 \leq 0.025$ and $\rho_-(x) = 0$ if $x_1 \geq -0.025$. The label of an input point x is $f^*(x) = \text{sgn}(x_1)$, which is the sign of its first coordinate.

We consider linear classifiers of the form $f(x) = \text{sgn}(w^{\top}x + b)$ trained with the cross-entropy loss $c((w, b), x, y) = \ln(1 + e^{-y(w^{\top}x + b)})$ where $y = f^*(x)$. We employ a one-step gradient method (which is an L_2 version of the fast gradient-sign method of Goodfellow et al., 2014; Papernot et al., 2016) to define our AEG g , which tries to modify a correctly classified point x with label y in the direction of the gradient of the cost function c : $x' = x + \varepsilon \nabla_x c((w, b), x, y) / \|\nabla_x c((w, b), x, y)\|_2$ for some $\varepsilon > 0$. For our specific choice of c , the above simplifies to $x' = x - \varepsilon y w / \|w\|_2$. To comply with the requirements for an AEG, we define g as follows: $g(x) = x'$ if $L(f, x) = 0$ and $f^*(x) = f^*(x')$ (corresponding to (G2) and (G1), respectively), while $g(x) = x$ otherwise. Therefore, if x' is misclassified by f , x and x' are the only points mapped to x' by g . Thus, the density at x' after the transformation g is $\rho'(x') = \rho(x) + \rho(x')(1 - L(f, x))\mathbb{I}(f^*(x) = f^*(x'))$ and

$$h_g(x') = \frac{\rho(x')}{\rho'(x')} = \frac{\rho(x')}{\rho(x') + \rho(x)(1 - L(f, x))\mathbb{I}(f^*(x) = f^*(x'))}$$

(note that $\mathbb{I}(L(f, x) = 0) = 1 - L(f, x)$).

We present two experiments showing the behavior of our independence test: one where the training and test sets are independent, and another where they are not.

In the first experiment a linear classifier was trained on a training set S_{Tr} of size 500 for 50,000 steps using the RMSProp optimizer (Tieleman and Hinton, 2012) with batch size 100 and learning rate 0.01, obtaining zero (up to numerical precision) final training loss c and, consequently, 100% prediction accuracy on the training data. Then the trained classifier was tested on a large test set S_{Te} of size 10,000.⁹ Both sets were drawn independently from ρ defined above. We used a range of ε values matched to the scale of the data distribution: from 10^{-2} , which is the order of magnitude of the margin between two classes (0.05), to 10^2 , which is the order of magnitude of the width of the Gaussian distribution used for each classes ($\sigma = \sqrt{500}$).

In the second experiment we consider the situation where the training and test sets are not independent. To enhance the effects of this dependence, the setup was modified to make the training process more amenable to overfitting by simulating a situation when the model has a wrong bias (this may happen in practice if

⁹The large number of test examples ensures that the random error in the empirical error estimate is negligible.

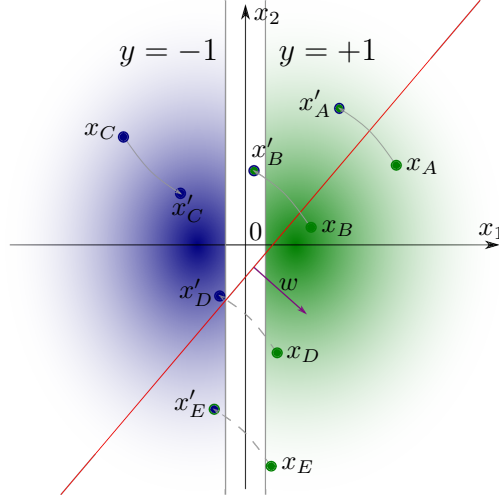


Figure 4: Illustration of the data distribution and the linear model $f(x) = \text{sgn}(w^\top x + b)$ in two dimensions. The blue and green gradients show the probability density ρ of the data with true labels $y = -1$ and $y = 1$, respectively, while the white space between them is the margin with $\rho = 0$. The red line is the model's classification boundary with its parameter vector w shown by the purple arrow. Depending on the label, w or $-w$ is the direction of translation used to perturb the correctly classified data points, and the translations used by the AEG g for specific points are depicted by grey arrows: solid arrows indicate the cases where $g(x) = x' \neq x$, while dashed arrows are for candidate translations which are not performed by the AEG because they would change the true label, $f^*(x') \neq f^*(x)$, and hence $g(x) = x \neq x'$. Each original/perturbed data point is represented by a color-coded circle: the inner color corresponds to the true label (dark blue for $y = -1$ and dark green for $y = 1$) while the outer color to the model's prediction (dark blue for $f(x) = -1$ and dark green for $f(x) = 1$). Points x'_A and x'_B can be obtained from x_A and x_B , respectively, by applying the AEG, $x'_A = g(x_A)$ and $x'_B = g(x_B)$. Since only x_A is mapped to x'_A by g , and $g(x'_A) = x'_A$, the density (Radon-Nikodym derivative) can be obtained as $h_g(x'_A) = \rho(x'_A)/(\rho(x_A) + \rho(x'_A)) \in (0, 1)$. In the case of x'_B , $h_g(x'_B) = \rho(x'_B)/(\rho(x_B) + \rho(x'_B)) = 0$ due to the margin. Note that the formula for $h_g(x'_A)$ does not depend on whether x_A or x'_A is in the original test set S ; in the first case we call x'_A a “successful adversarial example” while in the second case x'_A is called “originally misclassified” (a similar argument holds for $h_g(x'_B)$). x'_C is not a successful adversarial example since $L(f, x'_C) = 0$ (however, $g(x_C) = x'_C$ according to our definition). Points x_D and x_E are not perturbed by our AEG, since $f^*(x_D) \neq f^*(x'_D)$ and $f^*(x_E) \neq f^*(x'_E)$.

a wrong architecture or data preprocessing method is chosen, which, despite the modeler’s best intentions, worsens the performance). Specifically, during training we added a penalty term $10^4 w_1^2$ to the training loss c , decreased the size of the test set to 1000 and used 50% of the test data for training (the final penalized training loss was 0.25 with 100% prediction accuracy on the training set). Note that the small training set and the large penalty on w_1 yield classifiers that are essentially independent of the only interesting feature x_1 (recall that the true label of a point x is $\text{sgn}(x_1)$) and overfit to the noise in the data, resulting in a true model risk $R(f) \approx 1/2$.

The results of the two experiments are shown in Figure 5, plotted against different perturbation strengths: the left column corresponds to the first experiment while the right column to the second. The first row presents the p -values for rejecting the independence hypothesis, calculated by repeating the experiment (sampling data and training the classifier) 100 times and applying the single-model (Section 3, labelled as $N = 1$ in the plots) and N -model (Section 3.1, labelled as $N = 2, 10, 25, 100$ in the plots) independence test, and taking the average over models (or model sets of size N) for each ε . We also plot empirical 95% two-sided confidence intervals ($N \leq 2$) or, due to limited number of p -values available after dividing 100 runs into disjoint bins of size $N \geq 10$, ranges between minimum and maximum value ($N = 10, 25$). For all methods of detecting dependence, it can be seen that for the independent case the test is correctly not able to reject the independence hypothesis (the average p -value is very close to 1, although in some runs it can drop to as low as 0.5). On the other hand, for $10 \leq \varepsilon \leq 50$, the non-independent model failed the independence test at confidence level $1 - \delta \approx 100\%$, hence, in this range of ε our independence test reliably detects overfitting.

In fact, it is easy to argue that our test should only work for a limited range of ε , that is, it should not reject independence for too small or too large values of ε . First we consider the case of small ε values. Notice that except for points $g(x)$ ε -close (in L_2 -norm) to the true decision boundary or the decision boundary of f , $g(x)$ is invertible: if $g(x)$ is correctly classified and is ε -away from the true decision boundary, there is exactly one point, x , which is translated to $g(x)$, while if $g(x)$ is incorrectly classified and ε -away from the decision boundary of f , no translation leads to $g(x)$ and $x = g(x)$; any other points are ε -close to the decision boundary of either f or f^* . Thus, since ρ is bounded, $g(x)$ is invertible on a set of at least $1 - O(\varepsilon)$ probability (according to ρ). When $\varepsilon \rightarrow 0$, $g(x) \rightarrow x$, and so $\rho(g(x)) \rightarrow \rho(x)$ for all points x with $|x_1| \neq 0.025$ (since ρ is continuous in all such x), implying $h_g(g(x)) \approx 1$ on these points. It also follows that $L(f, x) \neq L(f, g(x))$ can only happen to a set of points with an $O(\varepsilon)$ ρ -probability. This means that $L(f, g(x))h_g(g(x)) \approx L(f, x)$ on a set of $1 - O(\varepsilon)$ ρ -probability, and for these points $T_g(x) = L(f, g(x))h_g(g(x)) - L(f, x) \approx 0$. Thus, $T_g(X) \approx 0$ with ρ -probability $1 - O(\varepsilon)$. Unless the test set S is concentrated in large part on the set of remaining points with $O(\varepsilon)$ ρ -probability, the test statistic $|T_{S,g}(f)| = O(\varepsilon)$ with high probability and our method will not reject the independence hypothesis for $\varepsilon \rightarrow 0$.

When ε is large ($\varepsilon \rightarrow \infty$), notice that for any point x with non-vanishing probability (i.e., with $\rho(x) > c$ for some $c > 0$), if $g(x) \neq x$ then $\rho(g(x)) \approx 0$. Therefore, for such an x , if $L(f, x) = 0$ and $L(f, g(x)) = 1$, $h_g(g(x)) = \rho(g(x))/(\rho(x) + \rho(g(x))) \approx 0$, and so $T_g(x) \approx 0$ (if $L(f, g(x)) = 0$, we trivially have $T_g(x) = 0$). If $L(f, x) = 1$, we have $g(x) = x$. If g is invertible at x then $h_g(x) = 1$ and $T_g(x) = 0$. If g is not invertible, then there is another x' such that $g(x') = x$; however, if $\rho(x) > c$ then $\rho(x') \approx 0$ (since ε is large), and so $h_g(g(x)) = \rho(x)/(\rho(x) + \rho(x')) \approx 1$, giving $T_g(x) \approx 0$. Therefore, for large ε , $T_g(X) \approx 0$ with high probability (i.e., for points with $\rho(x) > c$), so the independence hypothesis will not be rejected with high probability.

To better understand the behavior of the test, the second row of Figure 5 shows the empirical test error rate $\hat{R}_S(f)$, the (unadjusted) adversarial error rate $\hat{R}_{S'}(f)$, and the adversarial risk estimate $\hat{R}_g(f)$, together with their confidence intervals. For the non-independent model, we also show the expected error $R(f)$ (estimated over a large independent test set), while it is omitted for the independent model where it approximately coincides with both $\hat{R}_S(f)$ and $\hat{R}_g(f)$. While the reweighted adversarial error estimate $\hat{R}_g(f)$ remains the same for all perturbations in case of an independent test set (left column), the adversarial error rate $\hat{R}_{S'}(f)$ varies a lot for both the dependent and independent test sets. For example, in the case when the test samples and the model f are not independent, it undershoots the true error for $\varepsilon < 10$ and overshoots it for larger perturbations. For very large perturbations (ε close to 100), the behavior of $\hat{R}_{S'}(f)$ depends on the model f : in the independent case $\hat{R}_{S'}(f)$ decreases back to $\hat{R}_S(f)$ because such large perturbations

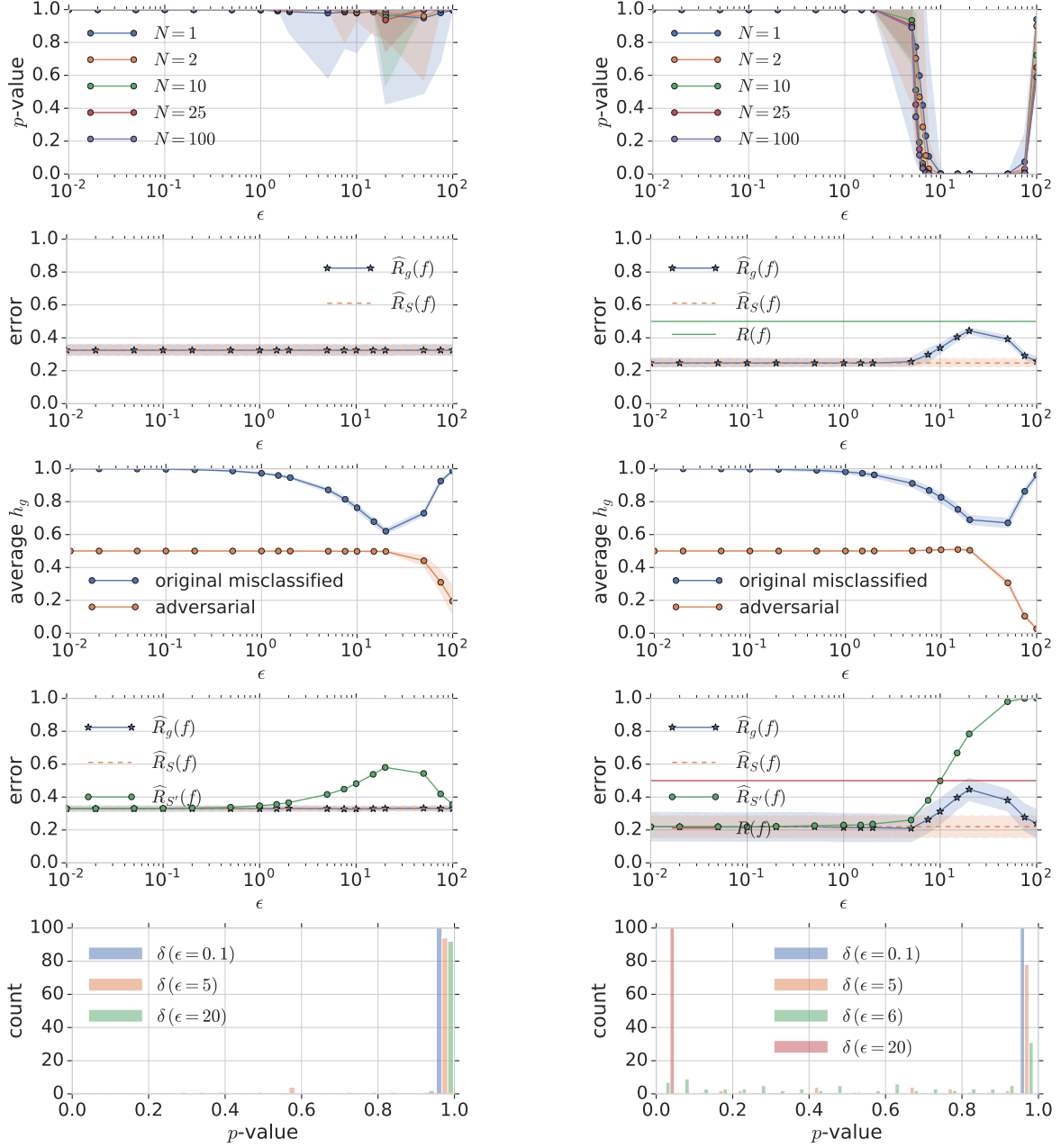


Figure 5: Risk and overfitting metrics for a synthetic problem with linear classifiers as a function of the perturbation strengths ϵ (log scale). Left: unbiased model tested on a large, independent test set (in this case $\hat{R}_S(f) \approx \hat{R}_g(f) \approx R(f)$); right: trained model overfitted to the test set ($\hat{R}_S(f) \leq \hat{R}_g(f)$ while both are smaller than $R(f)$). *First row:* Average p -value δ for the pairwise independence test with over 100 runs ($N = 1$) or the N -model independence test ($N > 1$). The bounds plotted are either empirical 95% two-sided confidence intervals ($N \leq 2$) or ranges between minimum and maximum value ($N = 10, 25$). *Second row:* Empirical two-sided 97.5% confidence intervals for the empirical test error rate $\hat{R}_S(f)$, the adversarial error rate $\hat{R}_{S'}$, and the adversarial risk estimate $\hat{R}_g(f)$. On the left, $R(f) \approx \hat{R}_S(f)$, while $R(f)$ is shown separately on the right. *Third row:* Average densities (Radon-Nikodym derivatives) for originally misclassified points and for the new data points obtained by successful adversarial transformations (with empirical 97.5% two-sided confidence intervals). *Fourth row:* The empirical test error rate $\hat{R}_S(f)$ and the adversarial risk estimate $\hat{R}_g(f)$ for a single realization with 97.5% two-sided confidence intervals computed from Bernstein's inequality, the adversarial error rate $\hat{R}_{S'}(f)$, and the expected error $R(f)$ (on the right, on the left $R(f) \approx \hat{R}_S(f)$). *Fifth row:* Histograms of p -values for selected ϵ values over 100 runs.

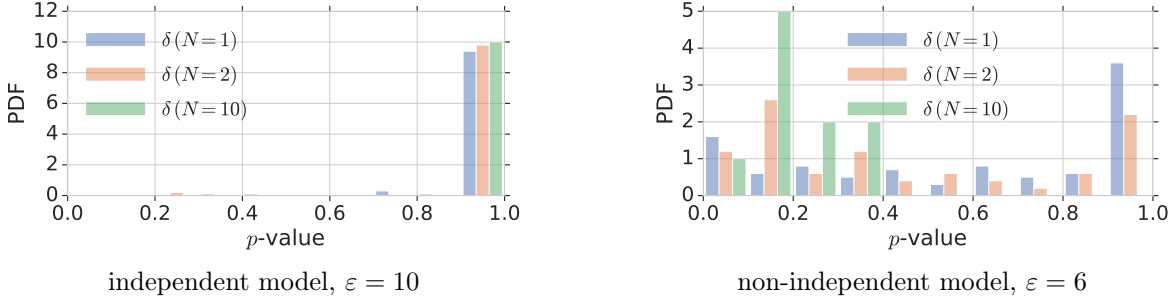


Figure 6: Histograms of p -values from N -model ($N = 1, 2, 10$) independence tests for both synthetic models and selected ε values, over 100 runs.

increasingly often change the true label of the original example, so less and less adversarial points are generated. In the case when the data and the model are not independent (right column), the adversarial perturbations are almost always successful (i.e., lead to a valid adversarial example for most originally correctly classified points), yielding an adversarial error rate close to one for large enough perturbations. This is because the decision boundary of f is almost orthogonal to the true decision boundary, and so the adversarial perturbations are parallel with the true boundary, almost never changing the true label of a point.

The plots of the densities (Radon-Nikodym derivatives), given in the third row of Figure 5, show how the change in their values compensate the increase of the adversarial error rate $\widehat{R}_{S'}(f)$: in the independent case, the effect is completely eliminated yielding an unbiased adversarial error estimate $\widehat{R}_g(f)$, which is essentially constant over the whole range of ε (as shown in the first row), while in the non-independent case the similar densities do not bring back the adversarial error rate $\widehat{R}_{S'}(f)$ to the test error rate $\widehat{R}_S(f)$, allowing the test to detect overfitting. Note that the densities exhibit similar trends (and values) in both cases, driven by the dependence of typical values of the $\rho(x)/\rho(g(x))$ ratio on the perturbation strength ε for originally misclassified points ($L(f, x) = 1$) and for successful adversarial examples (i.e., $L(f, x) = 0$ and $L(f, g(x)) = 1$).

To compare the behavior of our improved, pairwise test and the basic version, the fourth row of Figure 5 depicts a single realization of the experiments where the 97.5% confidence intervals (as computed from Bernstein’s inequality) are shown for the estimates. For the independent case, the confidence intervals of $\widehat{R}_S(f)$ and $\widehat{R}_g(f)$ overlap for all ε , and thus the basic test is not able to detect overfitting. In the non-independent case, the confidence intervals overlap for $\varepsilon = 10$ and $\varepsilon = 75$, thus the basic test is not able to detect overfitting with at a 95% confidence level, while the improved test (second row) is able to reject the independence hypothesis for these ε values at the same confidence level.

Finally, in the fifth row of Figure 5 we plotted the histograms of the empirical distribution of p -values for both models, over 100 independent runs (between the runs, all the data was regenerated and the models were retrained). For $\varepsilon = 0.1, 5, 20$, they concentrate heavily on either $\delta = 0$ or $\delta = 1$, and have very thin tails extending far towards the opposite end of the $[0, 1]$ interval. This explains the surprisingly wide 95% confidence intervals for p -values plotted in the first row. In particular, the fact that some p -values for the independent model are as low as 0.5 does not mean the independence test is not reliable, because almost all calculated δ values are close or equal to 1, and the few outliers are a combined consequence of the finite sample size and the effectiveness of the AEG. The additional $\varepsilon = 6$ histogram for the non-independent model illustrates a regime which is in between the single-model pairwise test (Section 3) completely failing to reject the independence hypothesis and clearly rejecting it.

To verify experimentally whether the N -model independence test can be a more powerful detector of overfitting than the single-model version, in Figure 6 (right panel) we plotted p -value histograms for $N = 1, 2, 10$ for the intermediate AEG strength $\varepsilon = 6$ applied to the non-independent model over 100 training runs. Indeed, as N increases, the concentration of p -values around in the low ($\delta \leq 0.2$) range increases. For

$N > 10$ we did not have enough values to plot a histogram: for $N = 25$ we obtained $\delta = 0.1851, 0.1599, 0.0661$ and 0.1941 , while for $N = 100$ the p -value is 0.1153 . The increase of the test power becomes apparent when we compare the last value with the mean of p -values obtained by testing every training run separately, equal 0.5984 , and the median 0.6385 .

For comparison, we also plotted in Figure 6 (left panel) the corresponding histograms for the independent model and a slightly higher attack strength, $\varepsilon = 10$, at which the independence tests fails for the overfitted model even without averaging (see Figure 5, first row, right panel). The histograms are all clustered in the δ region close to 1, indicating that the N -model test is not overly pessimistic.

5 Testing overfitting on image classification benchmarks

In the previous section we have shown how the proposed adversarial-example-based error estimates work for a synthetic problem where the densities (Radon-Nikodym derivatives) can be computed exactly. In this section we apply our estimates to two popular image datasets; here the main issue is to find sufficiently strong AEGs that allow computing the corresponding densities.

To facilitate the computation of the density h_g , we limit ourselves to density-preserving AEGs as defined by (G3) (recall that (G3) is different from requiring $h_g = 1$). Since in (4) and (5), $h_g(x)$ is multiplied by $L(f, x)$, we only need to determine the density h_g for data points that are misclassified by f .

5.1 AEGs based on translations

To satisfy (G3), we use translations of images as adversarial perturbations. Translation attacks have recently been proposed as means of generating adversarial examples (Azulay and Weiss, 2018). Although such attacks are relatively weak, they fit our needs well: unless the images are procedurally centered, it is reasonable to assume that translating them by a few pixels does not change their likelihood. When the images are procedurally centered, one can still run the test on the “neighboring distribution” where the centering is removed in a data augmentation procedure that applies random translations to the training data. Clearly, this (or for this matter translation attacks) will not work if centering is built into the prediction procedure, as it may happen if one’s goal is to build a model that is invariant to (small) translations. Since centering alone is not expected to provide a satisfactory solution to this invariance, we do not think that incorporating centering can be expected to be part of what a model does. As before, we only apply perturbations to correctly classified images. We also make the natural assumption that the small translations we use do not change the true class of an image. These assumptions imply that translations by a few pixels satisfy conditions (G1) and (G3), and so a function g is a valid AEG satisfying also (G3) if it leaves all misclassified images in place (to comply with (G2)), and either leaves a correctly classified image unchanged or applies a small translation.

Formally, images are modeled as 3D tensors in $[0, 1]^{W \times H \times C}$ space, where $C = 3$ for RGB data, and W and H are the width and height of the images, respectively. Let $\tau_v(x)$ denote the translation of an image x by $v \in \mathbb{Z}^2$ pixels in the (X, Y) plane (here \mathbb{Z} denotes the set of integers). To control the amount of change, we limit the magnitude of translations and allow $v \in \mathcal{V}_\varepsilon = \{u \in \mathbb{Z}^2 : u \neq (0, 0), \|u\|_\infty \leq \varepsilon\}$ only, for some fixed positive ε . Thus, we consider AEGs in the form $g(x) \in \{\tau_v(x) : v \in \mathcal{V}\} \cup \{x\}$ if $f(x) = f^*(x)$ and $g(x) = x$ otherwise (if x is correctly classified, we attempt to translate it to find an adversarial example in $\{\tau_v(x) : v \in \mathcal{V}\}$ which is misclassified by f , but x is left unchanged if no such point exists). Denoting the density of the pushforward measure \mathcal{P}_g by ρ_g , for any misclassified point x ,

$$\rho_g(x) = \rho(x) + \sum_{v \in \mathcal{V}} \rho(\tau_{-v}(x)) \mathbb{I}(g(\tau_{-v}(x)) = x) = \rho(x) \left(1 + \sum_{v \in \mathcal{V}} \mathbb{I}(g(\tau_{-v}(x)) = x) \right)$$

where the second equality follows from (G3). Therefore, the corresponding density is

$$h_g(x) = \frac{1}{1 + n(x)}, \quad (9)$$

where $n(x) = \sum_{v \in \mathcal{V}} \mathbb{I}(g(\tau_{-v}(x)) = x)$ is the number of neighboring images which are mapped to x by g . Note that given f and g , $n(x)$ can be easily calculated by checking all possible translations of x by $-v$ for $v \in \mathcal{V}$. It is easy to extend the above to non-deterministic perturbations, defined as distributions over AEGs, by replacing the indicator with its expectation $\mathbb{P}(g(\tau_{-v}(x)) = x | x, v)$ with respect to the randomness of g , yielding

$$h_g(x) = \frac{1}{1 + \sum_{v \in \mathcal{V}} \mathbb{P}(g(\tau_{-v}(x)) = x | x, v)} . \quad (10)$$

If g is deterministic, we have $h_g(x) \leq 1/2$ for any successful adversarial example x . Hence, for such g , the range U of the random variables T_i defined in (5) has a tighter upper bound of $3/2$ instead 2 (as $T_i \in [-1, 1/2]$), leading to a tighter bound in (6) and a stronger pairwise independence test. In the experiments, we use this stronger test.

For the image classification benchmarks we consider two translation variants that are used in constructing a translational AEG. For every correctly classified image x , we consider translations from \mathcal{V}_ε (for some ε), choosing $g(x)$ from the set $G(x) = \{\tau_v(x) : v \in \mathcal{V}_\varepsilon\} \cup \{x\}$. If all translations result in correctly classified examples, we set $g(x) = x$. Otherwise, we use one of two possible ways to select $g(x)$ (and we call the resulting points successful adversarial examples):

- *Strongest perturbation:* Assuming the number of classes is K , let $l(f, x) \in \mathbb{R}^K$ denote the vector of the K class logits calculated by the model f for image x , and let

$$l_{\text{exc}}(f, x) = \max_{0 \leq i < K} l_i(f, x) - l_y(f, x).$$

We define

$$g_{\text{strongest}}(x) = \operatorname{argmax}_{x' \in G(x)} l_{\text{exc}}(f, x'),$$

with ties broken deterministically by choosing the first translation from the candidate set, going top to bottom and left to right in row-major order. Thus, here we seek a non-identical “neighbor” that causes the classifier to err the most, reachable from x by translations within a maximum range ε .

- *Nearest misclassified neighbor:* Here we aim to find the nearest image in $G(x)$ that is misclassified. That is, letting $d(x, x') = \|v\|_2$ if $x' = \tau_v(x)$ and ∞ otherwise, we define

$$g_{\text{nearest}}(x) := \operatorname{argmin}_{x' \in G(x), L(f, x')=1} d(x, x')$$

with ties broken deterministically as above.

The two attack variants are successful on exactly the same set of images, hence they lead to the same adversarial error rates $\hat{R}_{S'}(f)$. However, they are characterized by different values of the density h_g and, consequently, yield different adversarial risk estimates $\hat{R}_g(f)$ and associated p -values for the independence test. The main difference between them is that the “strongest” version is more likely to map multiple images to the same adversarial example, thus decreasing the densities for successful adversarial examples and, counterintuitively, increasing them for originally misclassified points (as their neighbors are less likely to be mapped to these points).

To better see the effect of adversarial perturbations, we also consider two random baselines that do not take into account the success of a translation in generating misclassified points: $g_{\text{random}}(x)$ is chosen uniformly at random from $G(x) \setminus \{x\}$, and $g_{\text{random2}}(x)$ is chosen uniformly at random from $G(x)$.

5.2 ImageNet

First we apply our test to check if state-of-the-art classifiers for the ImageNet dataset (Deng et al., 2009) have been overfitted to the test set; recall that overfitting can happen by architecture or hyperparameter selection influenced by previous test outcomes. We use the VGG16 classifier architecture with its recommended input preprocessing (Simonyan and Zisserman, 2015). The preprocessing procedure involves rescaling every image

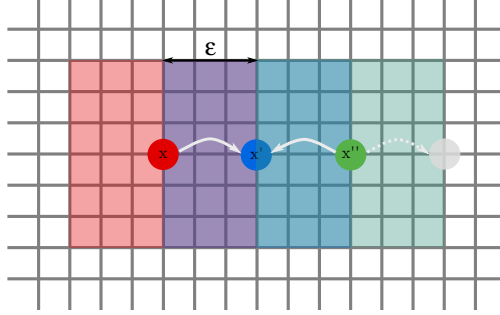


Figure 7: Image translations which need to be considered for a translational AEG with $\varepsilon = 3$. The red, blue and green balls represent the center of the original image x , adversarial example $x' = g(x)$ and another image x'' contributing to $\rho_g(x')$, respectively, while the semi-transparent squares of corresponding colors represent the possible translations which need to be considered for each of x , x' and x'' . Solid light grey arrows represent the relationships $x' = g(x)$ and $x' = g(x'')$. Finally, the dashed arrow and the semi-transparent grey ball represent an alternative mapping, which has to be ruled out while calculating the value of $g(x'')$ and, consequently, of $h_g(x')$. It is easy to see that the colored squares (which contain the translations needing to be evaluated) extend as far as 3ε from the original image x .

so that the smaller of width and height is 256 and next cropping centrally to size 224×224 . This means that translating the image by v can be trivially implemented by shifting the cropping window by $-v$ without any loss of information for $\|v\|_\infty \leq 16$, because we have enough extra pixels outside the original, centrally located cropping window. This allows us to compute the densities of the translational AEGs introduced in the previous subsection with $\|v\|_\infty \leq \varepsilon = \lfloor 16/3 \rfloor = 5$: in any direction, we may shift an image x by 5 pixels to generate adversarial examples x' , use translations by another 5 pixels to find the neighbors x'' of x' potentially contributing to $n(x')$ when computing $h_g(x')$, and finally another translation of x'' by at most 5 pixels to determine the exact value they contribute, that is, to compute the exact probabilities in (10) (see Figure 7 for an illustration). Because the ImageNet data collection procedure did not impose any strict requirements on centering the images (Deng et al., 2009), it is reasonable to assume (as we do) that lossless translations within these limits respect the density-preserving condition (G3).

Our first experiment demonstrates that our method is capable of detecting overfitting to the training set. We applied our pairwise independence test (6) to the training set with the above described translational AEGs applied to all 1,271,167 training examples, as well as to a number of its randomly selected (uniformly without replacement) subsets of different sizes. The left graph in Figure 8 shows that with the “strongest perturbation”, we were able to reject independence of the trained model and the training samples at a confidence level very close to 1 when enough training samples are considered (to be precise, for the whole training set the confidence level is 99.9994%). Note, however, that the much weaker “smallest perturbation” AEG, as well as the random transformations, are not able to detect the presence of overfitting. At the same time, the graph on the right hand side shows the relative strength of the pairwise independence test compared to the basic version based on independent confidence interval estimates as described in detail in Appendix A: the 97.5%-confidence intervals of the error estimates $\hat{R}_S(f)$ and $\hat{R}_g(f)$ overlap, not allowing to reject independence at a confidence level of 95% (note that here S denotes the training set).

In our second experiment, we applied the independence test to all 50,000 examples in the test set. Here we found that we could not reject the independence of the trained model and the test set at any positive confidence level for any translational AEG variant other than the “strongest perturbation”, for which we obtained a high p -value of 0.9593. Thus, we can conclude that, despite the iterative adaptation of the ImageNet classifier architectures and their training procedures to the same benchmark over the years (i.e., trying to minimize the ImageNet test set error rate), the resulting overfitting—if it exists at all—is too weak to be detected using our method and the tested perturbations.

There are many possible reasons for this result. The test may be too weak, as—similarly—no overfitting is detected to the training set at similar sample sizes, or perhaps there is no overfitting. The view of no

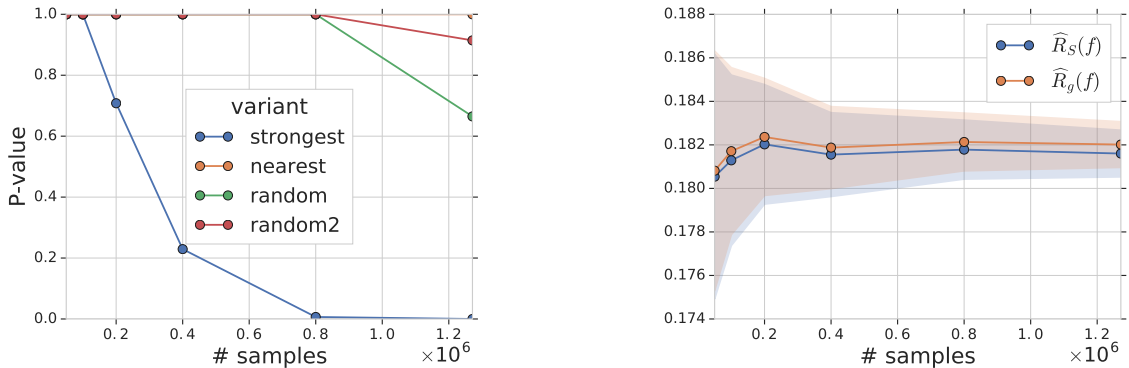


Figure 8: p -values for the independence test on the ImageNet training set for different sample sizes and AEG variants (left); original and adversarial risk estimates, $\widehat{R}_S(f)$ and $\widehat{R}_g(f)$, with 97.5% two-sided confidence intervals for the ‘strongest attack’ AEG (the adversarial error rate $\widehat{R}_{S'}(f)$ was approximately 7.7% larger than $\widehat{R}_S(f)$ for all sample sizes).

overfitting can be backed up in at least two ways: first, “manual” overfitting to the relatively *large* ImageNet test set is hard. Second, since training an ImageNet model was just too computationally expensive until quite recently, only a relatively small number of different architectures were developed for this problem, and the evolution of their design was often driven by computational efficiency on the available hardware, allowing the training of large networks on *any large image dataset*, not only by the goal of optimizing the performance for the fixed ImageNet test set.

5.3 CIFAR-10

We also applied our independence test to the CIFAR-10 dataset (Krizhevsky, 2009) and two recent neural network architectures that proved to be successful on this dataset.

5.3.1 Testing individual models

First we consider a VGG-like convolutional network model with architecture and training described in Section H.5 of Rosca et al. (2017). The model is trained with all images from the training and validation sets of the CIFAR-10 dataset (50,000 examples, referred to as training set in the rest of the section for simplicity). Unlike in the ImageNet case, translating the images here is not straightforward, since we do not have additional pixels outside of the original image boundaries (i.e., any translation would lead to loss of data and the ambiguity of what to use to pad the resulting empty space).

To alleviate this problem, we upsampled the images from 32×32 to size 44×44 , using bilinear sampling, and created a new training set by randomly selecting a 32×32 crop of each rescaled image (this allows us to translate, as in Section 5.2, central 32×32 crops of images by 6 pixels in every direction). Following the original procedure, during training we provided the model with random 24×24 crops sampled from the training images, while during test full size (32×32) images are used.¹⁰ In order to be able to apply translations, the test set was created from the central crops of the upsampled test images. We argue towards the end of this section that this preprocessing does not change the essential characteristics of the CIFAR-10 dataset.

To account for the variability of the randomized training process, as shown by the training and test set error rates, we repeated the training and evaluation procedure, including the independence test, 1250 times

¹⁰The convolutional filters’ weights are carried over from the training to the test phase, but the number of times each filter is applied at test time is larger than at training time. Average pooling applied before the final linear layer ensures that the latter can be the same in both training and test networks. The model was implemented in TensorFlow, see <https://tfhub.dev/deepmind/ganeval-cifar10-convnet/1> for an Open Source version.

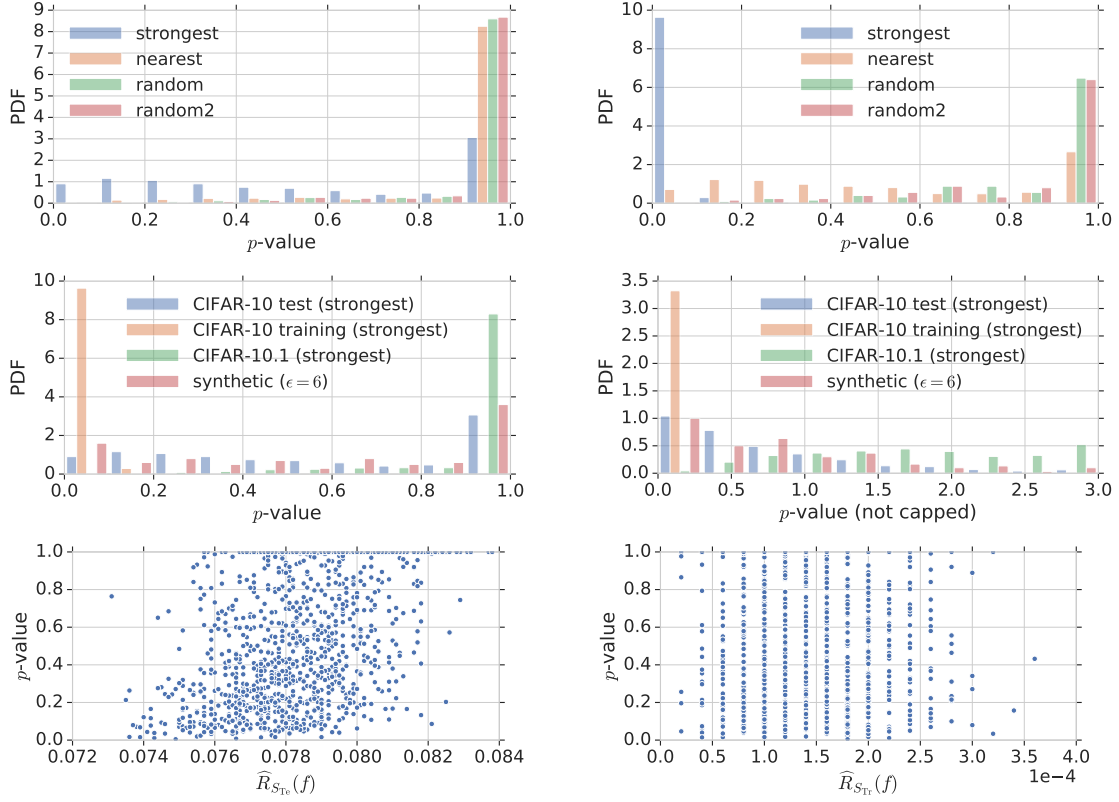


Figure 9: CIFAR-10 results for 1250 training runs on the rescaled training data. *First row:* Histograms of the p -values for the independence test applied to CIFAR-10 test (left panel) and training (right panel) set. *Second row:* Normalized histograms of the of p -values for the independence test with the VGG-like model trained on the cropped-upscaled CIFAR-10 dataset applied to the CIFAR-10 test and training sets and to the new CIFAR-10.1 test set (“strongest” AEG), as well as for the non-independent linear model from Section 4 (L_2 gradient attack with strength $\varepsilon = 6$), with (left panel) and without (right panel) capping the δ -values at 1 (see Equation (8)). *Third row:* Scatter plots of the p -values for the independence test (“strongest” AEG) applied to CIFAR-10 test set against the test (left panel) and training (right panel) set error rate.

(with the training and test sets kept fixed). The results of our experiments are summarized in Figure 9.

We applied the pairwise independence test (6) with translational AEGs from the previous section with $\varepsilon = 2$ pixels; the histogram of the resulting p -values for the test set and the centrally cropped training set are shown in the first row of Figure 9. Similarly to the previous case, only the “strongest” AEG detected overfitting to the training set (in almost all training runs and with mean p -value 0.023), hence, we use only this attack throughout the section. Accordingly, the other AEG methods also resulted in p -values largely concentrated around 1 on the test set, while the p -values of the “strongest” AEG are spread in the whole $[0, 1]$ interval, with about 25% of the runs resulting in a p -value 1 (where the independence could not be rejected at any confidence level), not allowing to convincingly accept or reject the independence of the model and the test set (some signs of overfitting are shown, e.g., the median p -value is ≈ 0.53 and the average is ≈ 0.56).

To understand this phenomenon better, we compared these values to the results of other independence tests. In particular, we performed the independence test of the trained models on the (similarly upscaled and cropped version of the) CIFAR-10.1 test set (Recht et al., 2018), a truly independent dataset collected recently following the CIFAR-10 selection principles. The resulting p -value histogram shows a completely different behavior, as the independence hypothesis could not be rejected at any positive confidence level for 998 out of 1250 training runs, while the remaining ones are distributed in a thin, long tail extending until

$p = 0.06$, with the overall mean p -value equal 0.93. Comparing the distributions of the p values, as presented on the left panel of the second row of Figure 9, we can see that the distribution of the p -values for the CIFAR-10 test set is somewhere in between the distributions from the independent CIFAR-10.1 test set and the overfitted CIFAR-10 training set. Comparing the “uncapped” p -values (obtained without capping the δ values in Equation (8) at 1), as shown on the right panel of the second row of Figure 9, we can identify the same effect. Note, however, that the CIFAR-10.1 test set is much smaller (2000 samples) than the CIFAR-10 test set (10000 samples), and our method is less capable of detecting overfitting at smaller sample sizes (see the left panel of Figure 8 for the ImageNet training set and Figure 11 in the next section for an overfitting test for the VGG-like architecture and the CIFAR-10 test set).

Comparing the CIFAR-10 histograms with the one for the non-independent linear model analyzed in Section 4, for L_2 gradient perturbation strength of $\varepsilon = 6$ suggests further evidence of overfitting. As can be seen in Figures 5 and 6, $\varepsilon = 6$ is in an intermediate regime between the regions where the independence test fails to reject the (known to be false) independence hypothesis, that is, when $\varepsilon \leq 5$, and where it does that reliably, that is, for $10 \leq \varepsilon \leq 50$. As shown in Figure 9, the histogram for the linear model and the one for the CIFAR-10 test set are quite similar (both with and without capping the p -values at 1), which suggests that the inability of the translational attacks to convincingly reject the independence of the CIFAR-10 test set and the trained models might be a result of the weakness of the translational attack, and that a stronger attack might be able to reject it conclusively.

To investigate whether the sometimes performed practice of “optimizing the random seed” (i.e., repeatedly retraining the model and choosing the training run with best performance metrics) can be detected by our independence test, we plotted the independence test p -values (on the test set) against the test and training error rates, $\hat{R}_{S_{Te}}(f)$ and $\hat{R}_{S_{Tr}}(f)$, in the third row of Figure 9. We observe very little correlation (1.49%) between δ and $\hat{R}_{S_{Tr}}(f)$, and just moderate one (49.41%) between δ and $\hat{R}_{S_{Te}}(f)$. Therefore, our independence test has a limited capability to detect test set overfitting via selection of the training run with the lowest test-set error rate. On the other hand, the scatter plot in the left panel of the third row of Figure 9 shows that almost all of the p -values corresponding to the lowest decile of test-set error rate values are below 0.5, and lower test error rates tend to correspond to lower p -values. However, no such connection can be made to the p -values (on the test set) and the training error rates.

5.3.2 Detecting overfitting for architectures

Based on the results for the synthetic problem presented in Section 4, we may expect that the N -model independence test (see Section 3.1) is a stronger detector of possible overfitting to the CIFAR-10 test set. Indeed, the plot on the left side of Figure 10 shows that as we average more models trained independently with the VGG-like architecture (i.e., larger N), the resulting p -values concentrate in the $\delta < 0.1$ range, similarly to the non-independent synthetic model results shown in Figure 6.¹¹ On the other hand, the corresponding histograms for the CIFAR-10.1 test set (right panel of Figure 10) do not exhibit this trend, with p -values clustered well above 50% for all N and concentrating in the 0.6–0.8 range for $N = 125$. For $N = 250, 625$ and 1250 , the p -values are around 0.03 for the CIFAR-10 test set and 0.7 for CIFAR-10.1 (since for these N ’s we did not have enough p -values—5, 2 and 1, respectively—to plot histograms, they are listed in Table 1). As N increases, the p_N values increasingly cluster around the $N = 1250$ value, $p_{1250} = 0.0281$, providing strong evidence for overfitting of the model architecture to the CIFAR-10 test set. In comparison, the corresponding values for the CIFAR-10.1 test set converge to about $p_{1250} = 0.6989$. Hence, the N -model dependence detector did not indicate overfitting in the case of a truly independent test set. Note, however, that directly comparing the behavior of the independence test on the CIFAR-10 and CIFAR-10.1 test sets is not entirely fair, as the sample size strongly affects the ability of our test to detect dependence (as we have already seen for the ImageNet training set in the left panel of Figure 8). Indeed, performing the independence test on subsets of the CIFAR-10 test set of similar sizes yields similar results as the ones we got for CIFAR-10.1. Varying the size of the subsets we use for testing, we can observe that the ability of our test to detect overfitting on the CIFAR-10 test set is seriously deteriorated for smaller sample

¹¹The test was always computed from our 1250 training runs, thus for every N we only have $1250/N$ p -values.

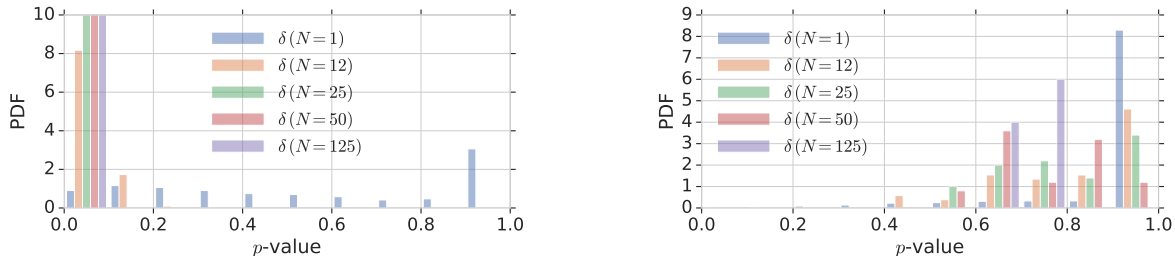


Figure 10: Histograms of p -values from N -model ($N = 1, 12, 25, 50, 125$) independence tests with the VGG-like architecture for the CIFAR-10 (left panel) and CIFAR-10.1 (right panel) test sets.

N	p_N for the CIFAR-10 test set	p_N for the CIFAR-10.1 test set
250	0.0266, 0.0274, 0.0283, 0.0292, 0.0359	0.6723, 0.6890, 0.7037, 0.7185, 0.7602
625	0.0267, 0.0303	0.6911, 0.7115
1250	0.0281	0.6989

Table 1: N -model p -values for the independence test with the VGG-like architecture on the CIFAR-10 (left) and the CIFAR-10.1 (right) test sets.

sizes (including size 2000, the size of the CIFAR-10.1 test set); this is shown in Figure 11.

We have applied the same procedure to another modern deep network architecture, the Wide Residual Network (WideResnet-28-10) of Zagoruyko and Komodakis (2016). We used the same data processing as for the VGG-like model and repeated the training process 125 times, resulting in 125 different models. The N -model test applied to the CIFAR-10 test set rejected the independence hypothesis with p -value 0.02445, which is an even stronger result than for the somewhat older VGG architecture (see Figure 12 for histograms of p -values from partially or not averaged models). Similar results were obtained for other WideResnet configurations, as shown in Table 2.¹² Note, however, that the p -values are not monotone functions of the test error rate, showing that the independence test is not fine-grained enough to detect slight differences in overfitting.

One may argue that our results are not relevant for the question if the architectures are overfitted to CIFAR-10 based on the grounds that the rescaled dataset is different from the original CIFAR-10 dataset. One argument against this is that since our tests were performed on a modified version of the original dataset, if anything, the models should show less overfitting than if they were trained and tested on the original CIFAR-10 dataset. Furthermore, as we show in the next subsection, the models trained on the original and the rescaled data are quite similar.

Therefore, we conclude that our results are relevant in assessing the overfitting of the VGG-like and the WideResnet architectures to CIFAR-10. They do not convincingly show overfitting for every training run (but neither do they overwhelmingly reject it), but after applying the multi-model independence test (of Section 3.1), the evidence becomes sufficiently strong to reject the independence hypothesis at a 97% confidence level. In previous work, Recht et al. (2018) argued that the fact that the test set error rates on CIFAR-10 and CIFAR-10.1 are highly correlated for a number of models indicates that there is no overfitting to the test set (since the CIFAR-10.1 test set is independent by construction). Our results provide a more refined assessment indicating that, when the randomness of the training procedure is “averaged away”, the evidence for the dependence between the model architectures and the CIFAR-10 test set is strong. A stronger attack, which still allows for an accurate estimation of the density, might be necessary to detect this dependence also at the level of individual training runs.

¹²Similarly to the models considered previously, the test error rates on our rescaled CIFAR-10 test set are a bit higher than the values reported by Zagoruyko and Komodakis (2016) for the original CIFAR-10 test set.

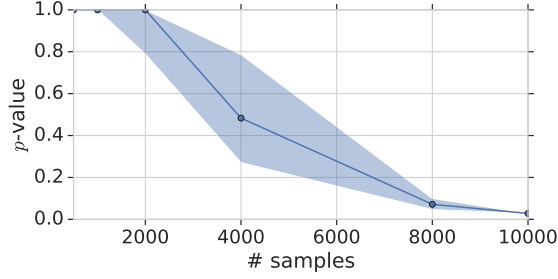


Figure 11: Average p -values for the N -model independence test with $N = 1250$ for the VGG-like architecture computed over random subsets of the CIFAR-10 test set with various sample sizes (plotted with two-sided 95% confidence intervals over 200 randomly selected subsets for each sample size).

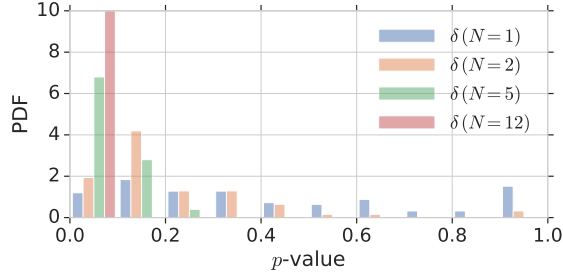


Figure 12: Histogram of p -values for the WideResnet architecture and “strongest” attack variant, for different numbers of models averaged together (CIFAR-10 test set).

5.3.3 Similarity of the models trained on the original and the rescaled CIFAR-10 datasets

In this section we provide quantitative evidence that the models trained on the original and the rescaled CIFAR-10 datasets have similar characteristics, hence our results are relevant to answer the question if the VGG-like architecture is overfitted to the original CIFAR-10 test set.

Training the VGG-like model 125 times on the original dataset yielded a test error rate of 5.52% (very close to the 5.48% reported originally by Rosca et al., 2017), while the performance of the 1250 models trained and tested on the cropped-upscaled dataset gave a substantially similar test error rate of 7.85% (over the different training runs), with an almost zero average error of 0.014% on the training data. The correlation between the models learned on the original and the rescaled and cropped datasets is also indicated by the fact that the average (again, over training runs) Jaccard index of the examples misclassified by either the model trained on the original data or the 1250 ones trained on the upscaled-cropped data is $J_b = 32.5\%$, while it should have been $J_{bi} = 3.33\%$ if the models had been independent. Additionally, in the 1250 sets of examples misclassified by both model trained on the original data and one of the models trained on rescaled-and-cropped data (median set size is $M_b = 327$), the incorrect labels generated by the compared models agree on average $L = 66.9\%$ of the points (median number of matching labels is $M_l = 219$), whereas an independent misclassification would have led to the models agreeing on approximately only 1/9-th of the jointly misclassified examples. Thus, we can conclude that not only do the models trained on the original and the rescaled CIFAR-10 datasets tend to classify correctly the same examples (showing the same objects, with or without rescaling), but they also tend to choose the incorrect label in a correlated way when they both misclassify a test example. This suggests that the two models would generalize to unseen examples (rescaled or not, resp.) in a similar way, and so conclusions about overfitting to the CIFAR-10 test set drawn from the analysis of the models trained on rescaled data should also be relevant for the case of models trained on original data.

For these reasons we believe that our results are relevant in assessing the overfitting of the VGG-like

model	test error rate (for non-rescaled CIFAR-10)	p_{125}
WideResnet-28-10	5.73% (4.17%)	0.024
WideResnet-22-10	5.80% (4.44%)	0.021
WideResnet-16-8	6.45% (4.81%)	0.033
WideResnet-40-2	7.24% (5.33%)	0.014

Table 2: Average test error rates and N -model p -values with $N = 125$ for different WideResnet architectures on the CIFAR-10 test set. The test error rates (in parentheses) for training and testing on the non-rescaled CIFAR-10 dataset are the ones presented in the original WideResnet paper of Zagoruyko and Komodakis (2016), trained and tested on the original CIFAR-10 dataset without rescaling.

architecture to CIFAR-10. They do not convincingly show overfitting for every training run (but neither do they overwhelmingly reject it), but after applying the multi-model independence test described in Section 3.1 the evidence becomes sufficiently strong to reject the independence hypothesis at a 97% confidence level.

Similar results are obtained for the WideResnet architectures: For example, for WideResnet-28-10, the mean test set error over 125 runs was 5.73%, compared to 4.2% when training and testing on non-rescaled data. The similarity metrics for this architecture were $J_b = 31.78\%$, $J_{bi} = 2.48\%$, $M_b = 240$, $L = 71.61\%$ and $M_l = 172$, which is similar to the values obtained above for the VGG-like architecture, and is evidence for the applicability of our method to WideResnet classifiers. Also note that, as shown in Table 2, the order of the relative performance of different WideResnet architectures is the same on the original and the rescaled CIFAR-10 dataset.

6 Conclusions

We presented a method for detecting overfitting of models to datasets. It relies on an importance weighted risk estimate from a new dataset obtained by generating adversarial examples from the original data points. We introduced the concept of adversarial example generators and showed how these can be used to derive an error estimate which is unbiased, and more interestingly, is guaranteed to have lower variance, and thus to be more reliable, than test error rates. Based on pairwise comparisons, we then introduced a test to detect overfitting to the test set. In synthetic experiments, we illustrated the method’s power. The synthetic example was chosen to simulate a case when the bias of the learning algorithm is incorrect (which we may expect when using weakly informed methods) and the algorithm needs to operate in a high-dimensional, low-data regime, the operating regime of most modern learning tasks. To check if overfitting does actually happens in practice, we applied our method to two popular image classification tasks, ImageNet and CIFAR-10. For this purpose, we proposed a variant of our general method that uses adversarial translations and argued for the correctness of this method. We did not detect overfitting in the case of ImageNet. However, we obtained strong evidence of overfitting to the CIFAR-10 test set for two recent model architectures (but not for individual training runs).

One limitation of our methods is that the applied translational attacks are quite weak, and it remains for the future to develop and try other tests that are based on other forms of attacks. Here, it is important to point out that the method developed for image classification is applicable to any other forms of attack as long as one can argue that the attack is density preserving. Thus, under this conditions, it should be possible to significantly increase the strength of the attacks, potentially leading to tests with significantly increased power (however, ensuring the density preserving property is not straightforward). If the set of possible adversarial modifications becomes large, the enumeration approach to calculate the importance weights may need to be adjusted. Another line of potential future research is to work out a version of our method that allows deviations between the densities before and after an AEG is applied, or relax the definition of AEGs and incorporate the resulting errors in the test. Yet another intriguing possibility to extend our method beyond density-preserving AEGs is to use the methods developed to estimate the importance weights directly based on data, or make use of other covariate shift adaptation methods (Sugiyama and Kawanabe, 2012; Yu and Szepesvári, 2012). It would also be interesting to consider extensions beyond image classification, for

example, by building on recent adversarial attacks for speech-to-text methods (Carlini and Wagner, 2018), machine translation (Ebrahimi et al., 2018a) or text classification (Ebrahimi et al., 2018b).

7 Acknowledgements

We thank J. Uesato for useful discussions and advice about adversarial attack methods and sharing their implementations (Uesato et al., 2018) with us, and M. Rosca for the help with retraining the CIFAR-10 model (Rosca et al., 2017). We also thank B. O’Donoghue for useful remarks about the manuscript, and D. Balduzzi, S. Legg, K. Kavukcuoglu and J. Martens for encouragement, support, lively discussions and feedback.

References

- Aharon Azulay and Yair Weiss. Why do deep convolutional networks generalize so poorly to small image transformations? 2018. arXiv:1805.12177.
- Dzmitry Bahdanau, Kyunghyun Cho, and Yoshua Bengio. Neural machine translation by jointly learning to align and translate. 2014. arXiv:1409.0473.
- Stéphane Boucheron, Gábor Lugosi, and Pascal Massart. *Concentration Inequalities: A Nonasymptotic Theory of Independence*. Oxford University Press, 2013.
- James Antonio Bucklew. *Introduction to Rare Event Simulation*. Springer New York, 2004.
- N. Carlini and D. Wagner. Audio adversarial examples: Targeted attacks on speech-to-text. In *2018 IEEE Security and Privacy Workshops (SPW)*, May 2018.
- Nicholas Carlini and David A. Wagner. Adversarial examples are not easily detected: Bypassing ten detection methods. In *Proceedings of the 10th ACM Workshop on Artificial Intelligence and Security, AISec@CCS 2017, Dallas, TX, USA, November 3, 2017*, pages 3–14, 2017a. URL <http://doi.acm.org/10.1145/3128572.3140444>.
- Nicholas Carlini and David A. Wagner. Towards evaluating the robustness of neural networks. In *2017 IEEE Symposium on Security and Privacy, SP 2017, San Jose, CA, USA, May 22-26, 2017*, pages 39–57, 2017b. URL <https://doi.org/10.1109/SP.2017.49>.
- Moustapha Cisse, Piotr Bojanowski, Edouard Grave, Yann Dauphin, and Nicolas Usunier. Parseval networks: Improving robustness to adversarial examples. In *Proceedings of the 34th International Conference on Machine Learning*, volume 70 of *Proceedings of Machine Learning Research*, pages 854–863, Sydney, Australia, 2017.
- J. Deng, W. Dong, R. Socher, L. J. Li, Kai Li, and Li Fei-Fei. ImageNet: A large-scale hierarchical image database. In *2009 IEEE Conference on Computer Vision and Pattern Recognition*, pages 248–255, June 2009. doi: 10.1109/CVPR.2009.5206848.
- L. Deng, G. Hinton, and B. Kingsbury. New types of deep neural network learning for speech recognition and related applications: an overview. In *2013 IEEE International Conference on Acoustics, Speech and Signal Processing*, pages 8599–8603. IEEE, May 2013.
- Cynthia Dwork, Vitaly Feldman, Moritz Hardt, Toniann Pitassi, Omer Reingold, and Aaron Roth. The reusable holdout: Preserving validity in adaptive data analysis. *Science*, 349(6248):636–638, 2015.
- Javid Ebrahimi, Daniel Lowd, and Dejing Dou. On adversarial examples for character-level neural machine translation. In *Proceedings of the 27th International Conference on Computational Linguistics, COLING 2018, Santa Fe, New Mexico, USA, August 20-26, 2018*, pages 653–663, 2018a.

- Javid Ebrahimi, Anyi Rao, Daniel Lowd, and Dejing Dou. Hotflip: White-box adversarial examples for text classification. In *Proceedings of the 56th Annual Meeting of the Association for Computational Linguistics, ACL 2018, Melbourne, Australia, July 15-20, 2018, Volume 2: Short Papers*, pages 31–36, 2018b.
- I. J. Goodfellow, J. Shlens, and C. Szegedy. Explaining and harnessing adversarial examples. 2014. arXiv:1412.6572.
- Alex Graves, Abdel-rahman Mohamed, and Geoffrey Hinton. Speech recognition with deep recurrent neural networks. In *2013 IEEE International Conference on Acoustics, Speech and Signal Processing*, pages 6645–6649. IEEE, 2013.
- Shixiang Gu and Luca Rigazio. Towards deep neural network architectures robust to adversarial examples. 2014. arXiv:1412.5068.
- Kaiming He, Xiangyu Zhang, Shaoqing Ren, and Jian Sun. Deep residual learning for image recognition. In *Proceedings of the IEEE Conference on Computer Vision and Pattern Recognition*, pages 770–778, 2016.
- H. Kahn and T. E. Harris. Estimation of particle transmission by random sampling. In *Monte Carlo Method*, volume 12 of *Applied Mathematics Series*, pages 27–30. National Bureau of Standards, 1951.
- J Zico Kolter and Eric Wong. Provable defenses against adversarial examples via the convex outer adversarial polytope. In *Proceedings of the 35th International Conference on Machine Learning*, volume 80 of *Proceedings of Machine Learning Research*, Stockholm, Sweden, 2017.
- Alex Krizhevsky. Learning multiple layers of features from tiny images. Technical report, University of Toronto, 2009.
- Alex Krizhevsky, Ilya Sutskever, and Geoffrey E Hinton. ImageNet classification with deep convolutional neural networks. In F. Pereira, C. J. C. Burges, L. Bottou, and K. Q. Weinberger, editors, *Advances in Neural Information Processing Systems 25*, pages 1097–1105. Curran Associates, Inc., 2012.
- Alex Kurakin and Ian Goodfellow. NIPS 2017: Defense against adversarial attack. <https://www.kaggle.com/c/nips-2017-defense-against-adversarial-attack>, 2017. Accessed: 2018-01-20.
- Fangzhou Liao, Ming Liang, Yinpeng Dong, Tianyu Pang, Jun Zhu, and Xiaolin Hu. Defense against adversarial attacks using high-level representation guided denoiser. 2017. arXiv:1712.02976.
- Aleksander Madry, Aleksandar Makelov, Ludwig Schmidt, Dimitris Tsipras, and Adrian Vladu. Towards deep learning models resistant to adversarial attacks. 2017. arXiv:1706.06083.
- Volodymyr Mnih, Csaba Szepesvári, and Jean-Yves Audibert. Empirical Bernstein stopping. In *Proceedings of the 25th International Conference on Machine Learning, ICML '08*, pages 672–679, New York, NY, USA, 2008. ACM.
- Nicolas Papernot, Patrick D. McDaniel, and Ian J. Goodfellow. Transferability in machine learning: from phenomena to black-box attacks using adversarial samples. 2016. arXiv:1605.07277.
- Nicolas Papernot, Patrick McDaniel, Ian Goodfellow, Somesh Jha, Z Berkay Celik, and Ananthram Swami. Practical black-box attacks against machine learning. In *Proceedings of the 2017 ACM on Asia Conference on Computer and Communications Security*, pages 506–519. ACM, 2017.
- Benjamin Recht, Rebecca Roelofs, Ludwig Schmidt, and Vaishal Shankar. Do CIFAR-10 classifiers generalize to CIFAR-10? 2018. arXiv:1806.00451.
- Mihaela Rosca, Balaji Lakshminarayanan, David Warde-Farley, and Shakir Mohamed. Variational approaches for auto-encoding generative adversarial networks. 2017. arXiv:1706.04987 and <https://tfhub.dev/deepmind/ganeval-cifar10-convnet/1>.

- K. Simonyan and A. Zisserman. Very deep convolutional networks for large-scale image recognition. In *International Conference on Learning Representations*, 2015.
- Masashi Sugiyama and Motoaki Kawanabe. *Machine Learning in Non-Stationary Environments – Introduction to Covariate Shift Adaptation*. MIT Press, 2012.
- Christian Szegedy, Wei Liu, Yangqing Jia, Pierre Sermanet, Scott Reed, Dragomir Anguelov, Dumitru Erhan, Vincent Vanhoucke, and Andrew Rabinovich. Going deeper with convolutions. In *2015 IEEE Conference on Computer Vision and Pattern Recognition (CVPR)*, 2015. arXiv:1409.4842.
- T. Tieleman and G. Hinton. Lecture 6.5—RmsProp: Divide the gradient by a running average of its recent magnitude. COURSERA: Neural Networks for Machine Learning, 2012.
- Florian Tramèr, Alexey Kurakin, Nicolas Papernot, Ian Goodfellow, Dan Boneh, and Patrick McDaniel. Ensemble adversarial training: Attacks and defenses. In *International Conference on Learning Representations*, 2018. arXiv:1705.07204.
- Jonathan Uesato, Brendan O’Donoghue, Aäron van den Oord, and Pushmeet Kohli. Adversarial risk and the dangers of evaluating against weak attacks. In *Proceedings of the 35th International Conference on Machine Learning*, volume 80 of *Proceedings of Machine Learning Research*, pages 5025–5034, 2018. arXiv:1802.05666.
- Yonghui Wu, Mike Schuster, Zhifeng Chen, Quoc V. Le, Mohammad Norouzi, Wolfgang Macherey, Maxim Krikun, Yuan Cao, Qin Gao, Klaus Macherey, Jeff Klingner, Apurva Shah, Melvin Johnson, Xiaobing Liu, Lukasz Kaiser, Stephan Gouws, Yoshikiyo Kato, Taku Kudo, Hideto Kazawa, Keith Stevens, George Kurian, Nishant Patil, Wei Wang, Cliff Young, Jason Smith, Jason Riesa, Alex Rudnick, Oriol Vinyals, Greg Corrado, Macduff Hughes, and Jeffrey Dean. Google’s neural machine translation system: Bridging the gap between human and machine translation. 2016. arXiv:1609.08144.
- Yaoliang Yu and Csaba Szepesvári. Analysis of kernel mean matching under covariate shift. In *29th International Conference on Machine Learning, (ICML)*, pages 607–614, 2012.
- Sergey Zagoruyko and Nikos Komodakis. Wide residual networks. 2016. arXiv:1605.07146.

A Basic version of the independence test

Under (H), standard concentration inequalities, such as the Chernoff or empirical Bernstein bounds (Boucheron et al., 2013), can be used to quantify how fast \widehat{R}_S and $\widehat{R}_g(f)$ concentrate around the expected error $R(f)$. In particular, we use the following empirical Bernstein bound (Mnih et al., 2008): Let $\bar{\sigma}_S^2 = (1/m) \sum_{i=1}^m (L(f, X_i) - \widehat{R}_S(f))^2$ and $\bar{\sigma}_g^2 = (1/m) \sum_{i=1}^m (L(f, g(X_i))h_g(g(X_i)) - \widehat{R}_g(f))^2$ denote the empirical variance of $L(f, X_i)$ and $L(f, g(X_i))h_g(g(X_i))$, respectively. Then, for any $0 < \delta \leq 1$, with probability at least $1 - \delta$,

$$|\widehat{R}_S(f) - R(f)| \leq B(m, \bar{\sigma}_S^2, \delta, 1) \quad (11)$$

where B is defined in (7) and we used the fact that the range of $L(f, x)$ is 1 (the last parameter of B is the range of the random variables considered). Similarly, with probability at least $1 - \delta$,

$$|\widehat{R}_g(f) - R(f)| \leq B(m, \bar{\sigma}_g^2, \delta, 1). \quad (12)$$

It follows trivially from the union bound that if the independence hypothesis (H) holds, the above two confidence intervals $[\widehat{R}_S(f) - B(m, \bar{\sigma}_S^2, \delta, 1), \widehat{R}_S(f) + B(m, \bar{\sigma}_S^2, \delta, 1)]$ and $[\widehat{R}_g(f) - B(m, \bar{\sigma}_g^2, \delta, 1), \widehat{R}_g(f) + B(m, \bar{\sigma}_g^2, \delta, 1)]$, which both contain $R(f)$ with probability at least $1 - \delta$, intersect with probability at least $1 - 2\delta$.

On the other hand, if f and S are not independent, the performance guarantees (11) and (12) may be violated and the confidence intervals may become disjoint. If this is detected, we can reject the independence hypothesis (H) at a confidence level $1 - 2\delta$ or, equivalently, with p -value 2δ . In other words, we reject (H) if the absolute value of the difference of the estimates $T_{S,g}(f) = \widehat{R}_g(f) - \widehat{R}_S(f)$ exceeds the threshold $B(m, \bar{\sigma}_S^2, \delta, 1) + B(m, \bar{\sigma}_g^2, \delta, 1)$ (note that $\mathbb{E}[T_{S,g}(f)] = 0$ if S and f are independent).